Available online at www.sciencedirect.com
SCIENCE DIRECT®
Journal of Computational Physics 212 (2006) 473–489
JOURNAL OF COMPUTATIONAL PHYSICS
www.elsevier.com/locate/jcp

Application of the lattice Boltzmann method to two-phase Rayleigh–Benard convection with a deformable interface

Qingming Chang, J. Iwan D. Alexander *

Department of Mechanical and Aerospace Engineering, National Center for Space Exploration Research, Case Western Reserve University, Glennan Building, Room 408, 10900 Euclid Avenue, Cleveland, OH 44106, USA

Received 26 November 2004; received in revised form 31 March 2005; accepted 23 May 2005
Available online 31 August 2005

Abstract

The lattice Boltzmann method (LBM) is extended to include the effects of interfacial tension and its dependence on temperature and is applied to the problem of buoyancy-driven flow in a non-isothermal two-phase system. No a priori assumptions are made regarding the shape and dynamic roles of the interface. The behavior of interface is obtained as part of the solution of the lattice Boltzmann equations. A parametric study of the effects of thermally induced density change, buoyancy, surface tension variation with temperature on interface dynamics, flow regimes and heat transfer is presented.

PACS: 76T05; 65C99

Keywords: The lattice Boltzmann method; Multiphase fluid flow; Rayleigh–Benard convection; Double distribution functions; Interface deformation; Boussinesq approximation; Marangoni force

1. Introduction

The Rayleigh–Benard system, in which a fluid is confined between two horizontal parallel plates and maintained at different temperatures, is one of the most studied non-equilibrium hydrodynamic systems.

Most prior work has focused on the case of a single fluid that fills the entire space between the plates [1–4]. However, there are systems of interest in which the fluid consists of two or more layers of immiscible liquids. Each fluid layer shares a common boundary with another fluid layer. Some previous numerical

* Corresponding author. Tel.: +1 216 368 0530; fax: +1 216 368 6445.
E-mail address: iwan@mae.cwru.edu (J.I.D. Alexander).

0021-9991/$ - see front matter
doi:10.1016/j.jcp.2005.05.031

studies [5–7] have been applied to the two-fluid Rayleigh–Benard problem but the shape of the interface was assumed to be rigid, flat and horizontal. Zhang and Alexander [8] have addressed the simpler computational problem of flows with curved deformable surfaces in liquid-bridge related problems. Cliffe and Tavener [9] employed an orthogonal mapping technique to solve the location of the deformable interface. However, to avoid the complex issues surrounding moving contact lines and time-dependent interfaces, they limited their studies to steady solutions.

Over the last decade, the lattice Boltzmann method (LBM) has become an established numerical approach in computer fluid dynamics (CFD), because of its capability to simulate flow in multiphase fluids. The underlying concept of the LBM is to incorporate the essential physics of the problem into a simplified kinetic equation such that the correct macroscopic behavior of the fluid is recovered. In contrast to traditional CFD methods which solve macroscopic equations, the LBM simulates fluid flow based on microscopic model or mesoscopic kinetic equations. This intrinsic feature is attractive to those who wish to incorporate microscopic or mesoscopic features and processes that are either not used in, or are difficult to incorporate, in traditional CFD simulation models. In particular, phase segregation and interfacial dynamics, which are essential in multiphase fluids are difficult (but not impossible) to simulate by traditional approaches, can be modeled in LBM by incorporation of molecular interactions. The sharp interface between different immiscible phases can be automatically maintained without any artificial treatment [10]. This feature is especially attractive when there is a need for modeling flow in so-called micro- or even nano-fluidic devices.

For simulating two-phase fluid flows, four LB methods have been used to date: the chromodynamic model proposed by Gunstensen et al. [11] and Grunau et al. [12], the pseudopotential model [13,14], the free-energy model proposed by Swift et al. [15,16] and the index fluid method developed by He [17]. All have their origins in kinetic theory. In some situations, the chromodynamic, pseudopotential and the free-energy model can lead to unphysical behavior, such as the spurious current around interfaces [18], thermodynamic inconsistencies [15] and lack of Galilean invariance [17,19]. The method recently developed by He and Chen [17] employs an index function to track different phases and the interface between them using a mean-field approximation for intermolecular attraction and Enskog's exclusion-volume effect for short range strong repulsion. When the molecular attraction is strong enough, the index function automatically separates into two different phases.

In most multiphase LBE models to date, only mass and momentum conservation is implemented. The macroscopic equations of these models correspond to the Navier–Stokes equation with an equation of state and a constant temperature. However, it is important and sometimes critical to have the capability of simulating thermal effects simultaneously with the fluid flow. Since the LBE method has several attractive features that make it a strong candidate for the simulation of complex fluids with multiple phases and phase transitions, it is necessary to develop the capability of simultaneously solving the energy, momentum and mass balance equations using LBM.

Unfortunately, the simulation of thermal multiphase systems by the LBE method has not yet achieved the same success as that of isothermal flows. Theoretically, a LBE model with energy conservation can be constructed [20–22] to yield a temperature evolution equation at the macroscopic level. However, when inter-particle forces are included, as in the multiphase models, energy conservation is further complicated by the contribution to the internal energy due to interactions between components. For this reason, constructing a non-ideal-gas LBE model with energy conservation is a challenge.

Rather than use a scheme for the energy balance that is based entirely on the LBM, we avoid the difficulties inherent in LBM and use a hybrid model that involves the LBM for the momentum and mass conservation equations and continuum model for the energy conservation. In other words, a two-phase LBM based on the double population model is combined with a scalar energy equation. Such an approach has been used by Filipova and Hanel [23] for instant to simulate combustion. Using the hybrid lattice Boltzmann finite-difference simulation, two-fluid Rayleigh–Benard convection is investigated. No a priori assumptions about the shape and dynamical behavior of the interface are made.

2. Two-phase model

The lattice Boltzmann method models fluid flow by simulating the behavior of the one-particle distribution function. The original Boltzmann equation describes the behavior of the one-particle distribution function, $f(\mathbf{r},\mathbf{e},t)$, which is defined as the density of the number of particles at point $\mathbf{r}$ at time t with a 'microscopic' velocity $\mathbf{e}$. If this function is known, the local macroscopic values of the fluid, such as density, momentum, temperature can be obtained by evaluating the moments of f. The other thermodynamic properties can then be calculated from the density and temperature through the equation of state.

To improve the stability of the simulation, the two-phase Boltzmann method proposed by He and Chen [17] was based on two distribution functions $f(\mathbf{r},\mathbf{e},t)$ and $g(\mathbf{r},\mathbf{e},t)$. In this scheme, $f(\mathbf{r},\mathbf{e},t)$ is an index distribution function that is used to track the density field, while $g(\mathbf{r},\mathbf{e},t)$ is the pressure distribution function which is needed to calculate both pressure and macroscopic velocity. The model is based on the Bhatnagar, Gross and Krook (BGK) approximation [24]

$$\partial_t f + \mathbf{e}\cdot\nabla_{\mathbf{r}} f = -\frac{f-f^{\mathrm{eq}}}{\tau} + \frac{(\mathbf{F}+\mathbf{G})\cdot(\mathbf{e}-\mathbf{u})}{\phi RT_0} f^{\mathrm{eq}}, \tag{1}$$

$$\partial_t g + \mathbf{e}\cdot\nabla_{\mathbf{r}} g = -\frac{g-g^{\mathrm{eq}}}{\tau} + (\mathbf{e}-\mathbf{u})\cdot[\Gamma(\mathbf{u})(\mathbf{F}+\mathbf{G}) - (\Gamma(\mathbf{u})-\Gamma(\mathbf{0}))\nabla\psi(\rho)]. \tag{2}$$

The second distribution function $g(\mathbf{r},\mathbf{e},t)$ is defined by

$$g(\mathbf{r},\mathbf{e},t) = f(\mathbf{r},\mathbf{e},t)RT_0 + \psi(\rho)\Gamma(\mathbf{0}) \tag{3}$$

and $\Gamma(\mathbf{u})$ is a function of the macroscopic velocity $\mathbf{u}$,

$$\Gamma(\mathbf{u}) = \frac{1}{(2\pi RT_0)^{\mathscr{D}/2}} \exp\left[-\frac{(\mathbf{e}-\mathbf{u})^2}{2RT_0}\right], \tag{4}$$

where $\mathscr{D} = 1, 2$ or 3 depending on the space dimension.

Here $\mathbf{F}$ and $\mathbf{G}$ are the effective molecular interaction and gravity force, respectively, R is the gas constant, T_0 is the reference temperature, in this paper (the average temperature $T_0 = (T_{\max} - T_{\min})/2$), ρ is the macroscopic fluid density, τ is the relaxation time and $\psi(\rho)$ is a density-dependent function to be specified later. The equilibrium distribution $f^{\mathrm{eq}}(\mathbf{r},\mathbf{e},t)$ satisfies the local Maxwell–Boltzmann equation [25,26]:

$$f^{\mathrm{eq}} = \frac{\phi}{(2\pi RT_0)^{\mathscr{D}/2}} \exp\left[-\frac{(\mathbf{e}-\mathbf{u})^2}{2RT_0}\right] = \phi\cdot\Gamma(\mathbf{u}). \tag{5}$$

From Eq. (3), equilibrium distribution $g^{\mathrm{eq}}(\mathbf{r},\mathbf{e},t)$ can be expressed in terms of $f^{\mathrm{eq}}(\mathbf{r},\mathbf{e},t)$ and $\Gamma(\mathbf{u})$

$$g^{\mathrm{eq}} = f^{\mathrm{eq}}RT_0 + \psi(\rho)\Gamma(\mathbf{0}) = \rho RT_0\Gamma(\mathbf{u}) + \psi(\rho)\Gamma(\mathbf{0}). \tag{6}$$

The effective molecular interaction force $\mathbf{F}$ can be expressed as the sum of two parts, a long range attractive force and short range repulsive one. These are expressed through a mean-field approximation and exclusion-volume effect that are taken to be

$$\mathbf{F} = \rho\nabla\mathscr{V} - B\rho^2RT_0\chi\nabla\ln(\rho^2\chi) = -\nabla(B\rho^2RT_0\chi - A\rho^2) + \kappa\rho\nabla\nabla^2\rho = -\nabla\psi + \mathbf{F}_{\mathrm{s}}. \tag{7}$$

Here $\mathbf{F}_{\mathrm{s}} = \kappa\rho\nabla\nabla^2\rho$ represents the force associated with surface tension, the parameter κ determines the strength of surface tension, $\psi = B\rho^2RT_0\chi - A\rho^2$ is related to the pressure by $\psi(\rho) = p - \rho RT_0$ and the pressure satisfies the following equation of state:

$$p = \rho RT_0(1 + B\rho\chi) - A\rho^2, \tag{8}$$

where B is related to the mass and effective diameter of a molecule, χ is the density-dependent collision probability for molecules, A and κ are constant and related to the intermolecular pair-wise potential u_{attr}.

The term $\nabla\psi$ in Eq. (7) depends on the equation of state, plays a key role in phase separation. In our study, the equation of state for Carnahan–Starling fluid is chosen. If setting $\chi = \frac{1-b\rho/8}{(1-b\rho/4)^3}$, the Carnahan–Starling equation of state can be rewritten in the form

$$p = \rho R T_0 \frac{1 + (b\rho/4) + (b\rho/4)^2 - (b\rho/4)^3}{(1 - b\rho/4)^3} - a\rho^2. \tag{9}$$

If the density gradient is small, the intermolecular attraction potential $\mathscr{V}$ can be expressed as

$$\mathscr{V} = -2A\rho - \kappa\nabla^2\rho. \tag{10}$$

Note that, this restricts the application of the model to fluids with similar densities situations such as gas–liquid interfaces cannot be tackled using this approximation.

The distribution function is discretized by representing the physical space with a discrete set of lattice points. The simplest sets of points coincide with the points on a regular lattice. The microscopic velocities associated with a given lattice point are represented by a finite number of velocity vectors to neighboring lattice points. In our study, a two-dimensional nine-velocity (D2Q9) model is employed. Here the physical space is represented by a square lattice. The corresponding velocity space at each point has eight velocity vectors, $\mathbf{e}_i$, $i = 1, 8$, that radiate out from the lattice point toward each of the nearest and next nearest neighbor points. The first velocity vector is zero vector at the lattice point, i.e., $\mathbf{e}_0 = \mathbf{0}$. Thus the velocity space is discretized to 9-speeds as below:

$$\mathbf{e}_i = \begin{cases} (0,0), & \alpha = 0, \\ (\sin\frac{\alpha\pi}{2}, -\cos\frac{\alpha\pi}{2})c, & \alpha = 1\text{–}4, \\ (\sin\frac{\alpha\pi}{2} + \cos\frac{\alpha\pi}{2}, \sin\frac{\alpha\pi}{2} - \cos\frac{\alpha\pi}{2})c, & \alpha = 5\text{–}8, \end{cases} \tag{11}$$

where $c^2 = 3c_s^2 = 3RT_0$, c_s is the so-called "LBM sound speed".

To solve the equations using an explicit scheme, a second-order accurate strategy is adopted to integrate the Boltzmann equations (1) and (2). This requires the following variable transformations:

$$\tilde{f} = f + \frac{(\mathbf{e} - \mathbf{u}) \cdot \nabla\psi(\phi)}{2RT_0} \Gamma(\mathbf{u})\delta t, \tag{12}$$

$$\tilde{g} = g - \tfrac{1}{2}(\mathbf{e} - \mathbf{u}) \cdot [\Gamma(\mathbf{u})(\mathbf{F}_s + \mathbf{G}) - (\Gamma(\mathbf{u}) - \Gamma(\mathbf{0}))\nabla\psi(\rho)]\delta t, \tag{13}$$

where δt is the time step.

When substituted into Eqs. (1) and (2), the discretized distribution functions $\tilde{f}_\alpha(\mathbf{r}, t)$ and $\tilde{g}_\alpha(\mathbf{r}, t)$ with microscopic velocity $\mathbf{e}_\alpha$ at a node site $\mathbf{r} + \mathbf{e}_\alpha\delta t$ at time $t + \delta t$, yield

$$\tilde{f}_\alpha(\mathbf{r} + \mathbf{e}_\alpha\delta t, t + \delta t) = \tilde{f}_\alpha(\mathbf{r}, t) + \frac{f_\alpha^{\text{eq}}(\mathbf{r}, t) - \tilde{f}_\alpha(\mathbf{r}, t)}{\tau/\delta t} - \frac{(2\tau - \delta t)}{2\tau} \frac{(\mathbf{e}_\alpha - \mathbf{u}) \cdot \nabla\psi(\phi)}{RT_0} \Gamma_\alpha(\mathbf{u})\delta t, \tag{14}$$

$$\begin{aligned} \tilde{g}_\alpha(\mathbf{r} + \mathbf{e}_\alpha\delta t, t + \delta t) = \tilde{g}_\alpha(\mathbf{r}, t) &+ \frac{g_\alpha^{\text{eq}}(\mathbf{r}, t) - \tilde{g}_\alpha(\mathbf{r}, t)}{\tau/\delta t} + \frac{(2\tau - \delta t)}{2\tau}(\mathbf{e}_\alpha - \mathbf{u}) \\ &\cdot [\Gamma_\alpha(\mathbf{u})(\mathbf{F}_s + \mathbf{G}) - (\Gamma_\alpha(\mathbf{u}) - \Gamma_\alpha(\mathbf{0}))\nabla\psi(\rho)]\delta t. \end{aligned} \tag{15}$$

The discrete equilibrium distribution function, is expressed in terms of Mach number u/c_s

$$f_\alpha^{\text{eq}} = w_\alpha\phi\left[1 + \frac{\mathbf{e}_\alpha \cdot \mathbf{u}}{c_s^2} + \frac{(\mathbf{e}_\alpha \cdot \mathbf{u})^2}{2c_s^4} - \frac{\mathbf{u}^2}{2c_s^2}\right] = \phi \cdot \Gamma_\alpha(\mathbf{u}), \tag{16}$$

$$g_\alpha^{\mathrm{eq}} = w_\alpha\left[p + \rho RT_0\left(\frac{\mathbf{e}_\alpha\cdot\mathbf{u}}{c_s^2} + \frac{(\mathbf{e}_\alpha\cdot\mathbf{u})^2}{2c_s^4} - \frac{\mathbf{u}^2}{2c_s^2}\right)\right] = w_\alpha(p-\rho RT_0) + \Gamma_\alpha(\mathbf{u})\rho RT_0, \tag{17}$$

$$\Gamma_\alpha(\mathbf{u}) = w_\alpha\left[1 + \frac{\mathbf{e}_\alpha\cdot\mathbf{u}}{c_s^2} + \frac{(\mathbf{e}_\alpha\cdot\mathbf{u})^2}{2c_s^4} - \frac{\mathbf{u}^2}{2c_s^2}\right], \tag{18}$$

where w_α is the integral weight.

$$[w_0, w_1, w_2, w_3, w_4, w_5, w_6, w_7, w_8] = \left[\frac{4}{9}, \frac{1}{9}, \frac{1}{9}, \frac{1}{9}, \frac{1}{9}, \frac{1}{36}, \frac{1}{36}, \frac{1}{36}, \frac{1}{36}\right]. \tag{19}$$

Finally, the hydrodynamic variables, the density of the index fluid ϕ, the pressure p and the macroscopic velocity u, can be calculated as kinetic moments of $\tilde{f}_\alpha(\mathbf{r},t)$ and $\tilde{g}_\alpha(\mathbf{r},t)$:

$$\phi = \sum_{\alpha=0}^{8}\tilde{f}_\alpha, \tag{20}$$

$$p = \sum_{\alpha=0}^{8}\tilde{g}_\alpha - \frac{1}{2}\mathbf{u}\cdot\nabla\psi(\rho)\delta t, \tag{21}$$

$$\mathbf{u} = \frac{1}{\rho c_s^2}\sum_{\alpha=0}^{8}\mathbf{e}_\alpha\tilde{g}_\alpha + \frac{\delta t}{2\rho}(\mathbf{F}_s + \mathbf{G}). \tag{22}$$

The real fluid density and viscosity can be calculated from the index function ϕ

$$\rho(\phi) = \rho_l + \frac{\phi-\phi_l}{\phi_h-\phi_l}(\rho_h-\rho_l), \tag{23}$$

$$v(\phi) = v_l + \frac{\phi-\phi_l}{\phi_h-\phi_l}(v_h-v_l). \tag{24}$$

Here ρ_l and ρ_h are the densities of the light and heavy fluids, respectively; v_l and v_h are viscosities of light and heavy fluids, respectively; ϕ_l and ϕ_h are the minimum and maximum values of the index function.

Assuming that the Boussinesq approximation holds for each fluid, all the fluid properties are considered as constant, except the body force term in Eqs. (2) and (13), where the fluid density is assumed $\rho = \rho_{\mathrm{avg}}[1-\beta_i(T-T_0)]$. The effective additional thermal buoyancy force can be written as

$$\mathbf{G}_{\mathrm{tb}} = \rho_{\mathrm{avg}}[1-\beta_i(T-T_0)]\mathbf{g}, \tag{25}$$

where T_0 is set to be the average value of the hot wall and cold wall temperatures, $T_0 = \frac{1}{2}(T_h + T_c)$.

An additional body force term arises due to the phase buoyancy force related to the density jump across a phase boundary caused by different phases can be given as

$$\mathbf{G}_{\mathrm{pb}} = (\rho - \rho_{\mathrm{avg}})\mathbf{g}, \tag{26}$$

where ρ_{avg} is the average density of two equilibrium phases.

3. Incorporation with thermodynamics

Most of the published LBM multiphase studies have been restricted to isothermal systems [13,15–17,19,20]. Consensus has yet to be reached as to how to self-consistently incorporate all thermodynamic quantities (internal kinetic and potential energy, free-energy, entropy, etc.). The most obvious difficulty

is tracking the energy evolution while conserving total energy. This means, that the kinetic model is required not only to recover the correct mass and momentum equations, but also the energy equation.

In what follows, we introduce a model that couples a multiphase LBM with the macroscopic energy equation. The thermal multiphase fluid dynamics is separated to two parts, fluid dynamics and thermal dynamics. Momentum and mass balance is determined by isothermal multiphase LBM-scheme while the energy balance is governed by a scalar energy conservation equation and modeled by differential-scheme.

The energy transport in macroscopic level satisfies

$$\partial_t(\rho e) + \nabla\cdot(\rho \mathbf{u} e) = -p\nabla\cdot\mathbf{u} + \Pi : \nabla\mathbf{u} - \nabla\cdot\mathbf{q}, \tag{27}$$

where e represents the specific internal energy, $\mathbf{q}$ represents the heat flux vector, the first term on the right-hand side is the work done by pressure, and the second term on the right-hand is the dissipation term in which Π represents the stress tensor.

For a multiphase system, we further split Π in Eq. (27) into two parts, $\Pi = \Pi_1 + \Pi_2$, one represents the viscous stress tensor Π_1, the other an effective interfacial stress tensor Π_2. They are assumed to have the form

$$\Pi_1 = \rho\nu(\nabla\mathbf{u} + \mathbf{u}\nabla), \tag{28}$$

$$\Pi_2 = \left(\kappa\rho\nabla^2\rho + \frac{\kappa}{2}|\nabla\rho|^2\right)\mathbf{I} - \kappa\nabla\rho\nabla\rho. \tag{29}$$

Note that, the form of Π_2 is similar in form to the so-called Korteweg stress in an isotropic two-phase immiscible fluid system [27].

The internal energy can be expressed as

$$e = c_v T, \tag{30}$$

where c_v is the specific heat at constant volume and T is the fluid temperature.

The heat flux $\mathbf{q}$ is assumed to follow Fourier's law:

$$\mathbf{q} = -k\nabla T, \tag{31}$$

where k is the thermal conductivity of fluid.

Assuming thermal conductivity k and specific heat c_v are constant, Eq. (27) can be regrouped and the following system of equations and boundary conditions is solved:

$$\begin{aligned} c_v[\partial_t(\rho T) + \nabla\cdot(\rho T\mathbf{u})] = {} & -p\nabla\cdot\mathbf{u} + k\nabla^2 T + \rho\nu(\nabla\mathbf{u} + \mathbf{u}\nabla) \\ & : \nabla\mathbf{u} + \left[\kappa\rho\nabla^2\rho + \frac{\kappa}{2}|\nabla\rho|^2\right]\nabla\cdot\mathbf{u} - \kappa\nabla\rho\nabla\rho : \nabla\mathbf{u}. \end{aligned} \tag{32}$$

Eq. (32) is solved simultaneously with the following equations for the distribution functions $\tilde{f}_\alpha$ and $\tilde{g}_\alpha$:

$$\tilde{f}_\alpha(\mathbf{r} + \mathbf{e}_\alpha\delta t, t + \delta t) = \tilde{f}_\alpha(\mathbf{r}, t) + \frac{f_\alpha^{\mathrm{eq}}(\mathbf{r}, t) - \tilde{f}_\alpha(\mathbf{r}, t)}{\tau/\delta t} - \frac{(2\tau - \delta t)}{2\tau}\frac{(\mathbf{e}_\alpha - \mathbf{u})\cdot\nabla\psi(\phi)}{RT_0}\Gamma_\alpha(\mathbf{u})\delta t, \tag{33}$$

$$\begin{aligned} \tilde{g}_\alpha(\mathbf{r} + \mathbf{e}_\alpha\delta t, t + \delta t) = {} & \tilde{g}_\alpha(\mathbf{r}, t) + \frac{g_\alpha^{\mathrm{eq}}(\mathbf{r}, t) - \tilde{g}_\alpha(\mathbf{r}, t)}{\tau/\delta t} + \frac{(2\tau - \delta t)}{2\tau}(\mathbf{e}_\alpha - \mathbf{u}) \\ & \cdot [\Gamma_\alpha(\mathbf{u})(\mathbf{F}_s + \mathbf{G}) - (\Gamma_\alpha(\mathbf{u}) - \Gamma_\alpha(\mathbf{0}))\nabla\psi(\rho)]\delta t, \end{aligned} \tag{34}$$

and macroscopic variables

$$\phi = \sum_{\alpha=0}^{8}\tilde{f}_\alpha, \tag{35}$$

$$p = \sum_{\alpha=0}^{8} \tilde{g}_\alpha - \frac{1}{2}\mathbf{u}\cdot\nabla\psi(\rho)\delta t, \tag{36}$$

$$\mathbf{u} = \frac{1}{\rho c_s^2}\sum_{\alpha=0}^{8}\mathbf{e}_\alpha\tilde{g}_\alpha + \frac{\delta t}{2\rho}(\mathbf{F}_s + \mathbf{G}). \tag{37}$$

Non-slip (bounce-back) boundary conditions are employed at the top and bottom walls and periodic boundary conditions are used to in the horizontal direction in this paper.

Note that, even though each of the fluid phases is incompressible, the density ρ in Eq. (32) (which represents a two-phase system) cannot be treated as a constant because there is a sharp density gradient at the interface between the two phases. Furthermore, the density gradient contributes to the interfacial stresses that are manifested as a surface tension.

Accordingly, the velocity, pressure, density and temperature fields are solved at each time step as follows:

(a) Set an initial velocity $\mathbf{u}$, density ρ, index function ϕ, pressure p and temperature T at each site in the domain field.
(b) Calculate the buoyancy forces $\mathbf{G}_{tb}$ and $\mathbf{G}_{pb}$ using (25) and (26), respectively.
(c) Based on the values of $\mathbf{u}$, ρ, ϕ, p and $\mathbf{G}$, calculate equilibrium distributions $f_\alpha^{eq}(\mathbf{r},t)$, $g_\alpha^{eq}(\mathbf{r},t)$ with (16)–(18) at each site; complete the collision and propagation by (33), (34) to obtain distribution functions $\tilde{f}_\alpha(\mathbf{r},t)$, $\tilde{g}_\alpha(\mathbf{r},t)$ at the new time step.
(d) Calculate ϕ, p, $\mathbf{u}$ and ρ with (35)–(37) and (23) at the new time step.
(e) Solve the new temperature field using the energy equation (32).
(f) Return to step (b) and repeat until either a steady state is obtained or, for time-dependent flows, until the desired time has elapsed.

Using the numerical procedures outlined above, the hybrid thermal LBM couples the LB momentum equations with the macroscopic energy equation through the introduction of a macroscopic Boussinesq buoyancy force in the momentum equation.

4. Numerical simulation of Rayleigh–Benard convection of a two-layer fluid system

The Rayleigh–Benard convection has been studied extensively and, thus, serves as an excellent benchmark for our LBM simulation. We consider two horizontal layers of immiscible fluid, confined between

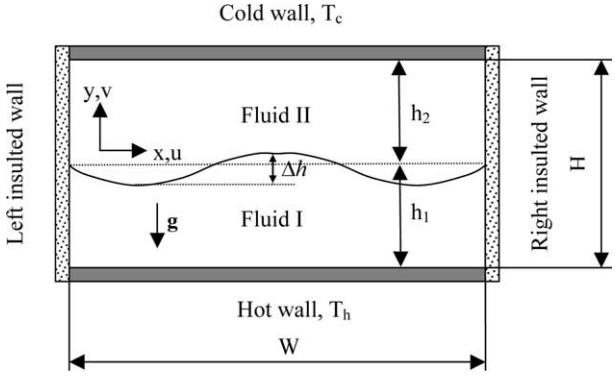

Fig. 1. Schematic of the two-fluid system.

rigid isothermal plates kept at different temperatures. As shown in Fig. 1, two rigid parallel isothermal plates at constant temperature bound a system of two immiscible fluids that share an interface. The Cartesian coordinates are such that x is horizontal and the gravity vector is antiparallel to its y-axis.

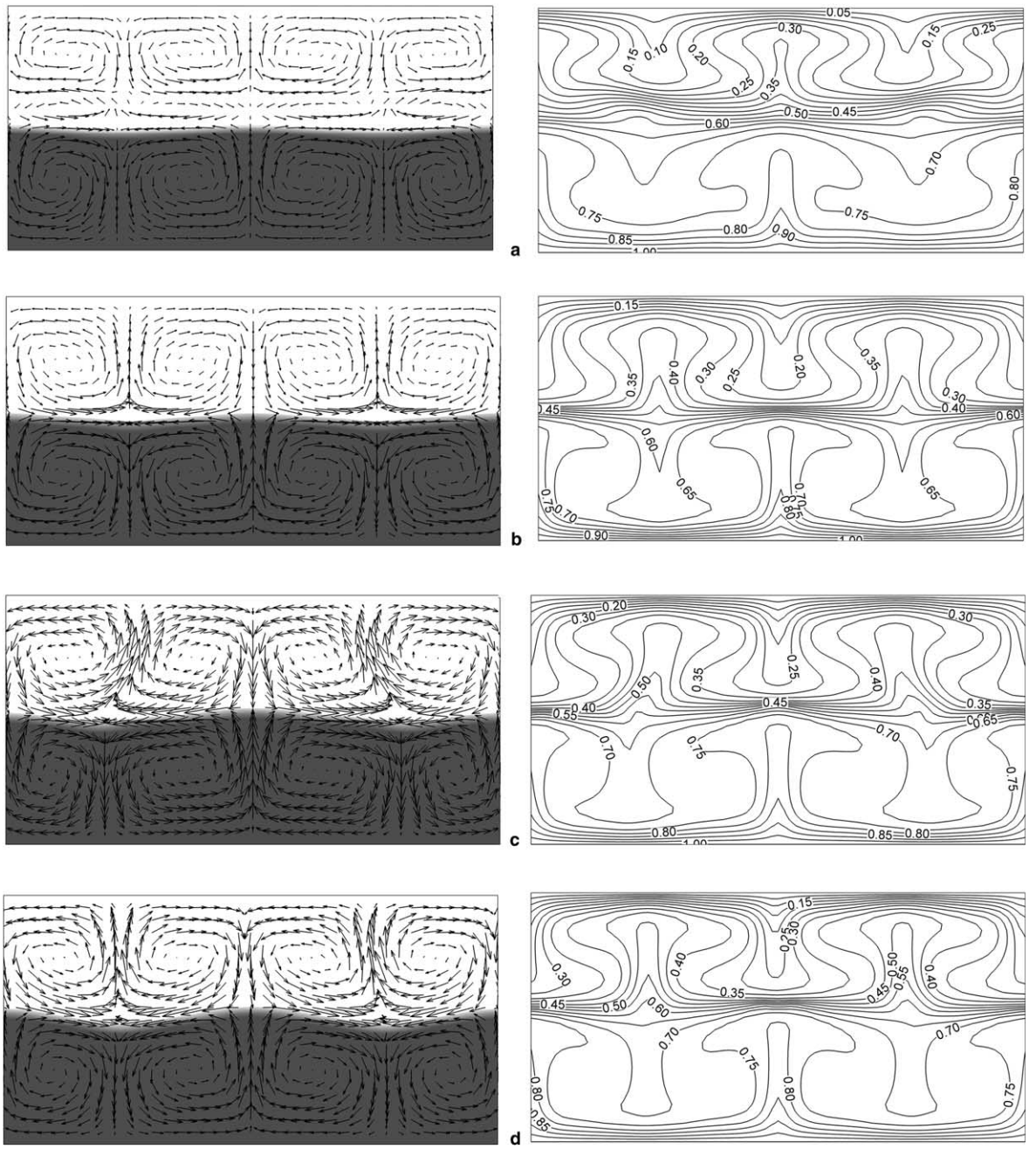

Fig. 2. Flow and thermal fields for $Ra_1 = 8.0 \times 10^4$, $Ca_1 = 4.6 \times 10^{-4}$ and $Ma_1 = 0$: (a) $\varepsilon_1 = 0.0667$, (b) $\varepsilon_1 = 0.10$, (c) $\varepsilon_1 = 0.15$ and (d) $\varepsilon_1 = 0.20$.

Each fluid is characterized by its thickness h_i, thermal conductivity k_i, specific heat c_{vi}, volumetric mass density ρ_i, kinematic viscosity v_i and thermal expansion coefficient β_i. The subscript $i = 1$ refers to lower layer fluid I, $i = 2$ to the upper layer fluid II. Unless otherwise stated, the ratio of physical properties of the fluid II to fluid I have been fixed as $\rho_r = 0.33$, $\beta_r = 2.0$, $k_r = 0.7$, $c_{vr} = 0.4$, $v_r = 1.0$. Initially, a two-layer system of immiscible fluids at equal depth, $h_1 = h_2 = 0.5H$, fills the cavity with width W and height H. The aspect ratio of the enclosed cavity W/H was selected as 2:1 and the simulation was carried out on an 81 by 41 grid. We also recalculated selected cases with a 161 by 81 grid. The results are close. For the case presented in Fig. 2(b), for example, the maximum velocity magnitude difference is only 2.1%. The location of the maximum and minimum velocities was less than 1.0% error, indicating the grid is sufficiently well resolved.

The important non-dimensional parameters of this problem are the Rayleigh number $Ra_1 = g\beta_1\Delta THPr_1/v_1^2$, Capillary number $Ca_1 = \rho_1 v_1 u_{ref}/\sigma = \rho_1 v_1\sqrt{g\beta_1 H\Delta T}/\sigma$, the Marangoni number $Ma_1 = (\partial\sigma/\partial T)\Delta TH/(\rho_1 v_1\alpha_1) = \gamma\Delta TH/(\rho_1 v_1\alpha_1)$ and $\varepsilon_1 = \beta_1\Delta T$, where $\Delta T = T_h - T_c$ is the temperature difference between the hot and cold walls, and the Prandtl number is $Pr_1 = v_1/\alpha_1$, where $\alpha = k/(\rho c_v)$ is the thermal diffusivity.

In the first case, we fixed $Ra_1 = 8.0\times10^4$, $Ca_1 = 4.6\times10^{-4}$ and neglected surface tension forces arising from a temperature dependence of κ in Eq. (7), i.e., ($Ma_1 = 0$), which is designed to demonstrate how the flow, thermal characteristics and deformation of the interface are altered by the parameter ε_1.

The flow features of a two-layered convection are captured in Fig. 2. Each layer is occupied by clockwise and counterclockwise circulating cells and the circulating in the upper layer is little weaker that in the lower layer.

It is seen, as expected, that the deformation of interface increases as ε_1 increases, as shown in Fig. 3. In this plot, deformation rate represents the interface deformation over cavity height, $\Delta h/H$. The deformation rate is less than 3.0% if $\varepsilon_1 < 0.10$, which is relatively small and could become unappreciable. However, when ε_1 takes large value, the interface deformation cannot be neglected. Fig. 4 shows the evolution of fluid convection caused by thermal buoyancy force in case of $\varepsilon_1 = 0.26$ at some representative dimensionless time, where we take $t = \sqrt{H/(g\beta\Delta T)}$ as the time scale.

The effect of Rayleigh number Ra_1 on the interface deformation and heat transfer coefficient is shown in Fig. 5. In this case, we fixed $\varepsilon_1 = 0.15$, $Ca_1 = 4.6\times10^{-4}$ and neglected Marangoni force ($Ma_1 = 0$). In each case, there are two pairs of counter-rotating convection rolls both in lower layer and in upper layer. As

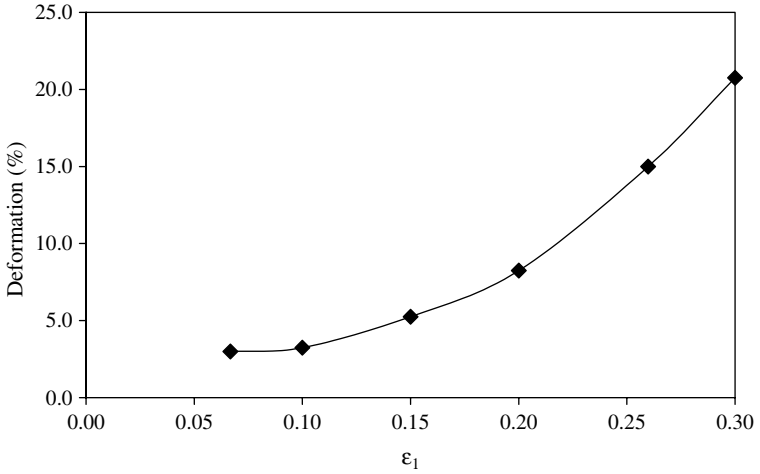

Fig. 3. Interface deformation vs. ε_1 $Ra_1 = 8.0\times10^4$,$Ca_1 = 4.6\times10^{-4}$ and $Ma_1 = 0$.

Rayleigh number increases, the fluid convection become stronger and the isotherms are more distorted. However, the interface deformation does not appear to be affected by changes in the Rayleigh number. This can also be observed in Fig. 6.

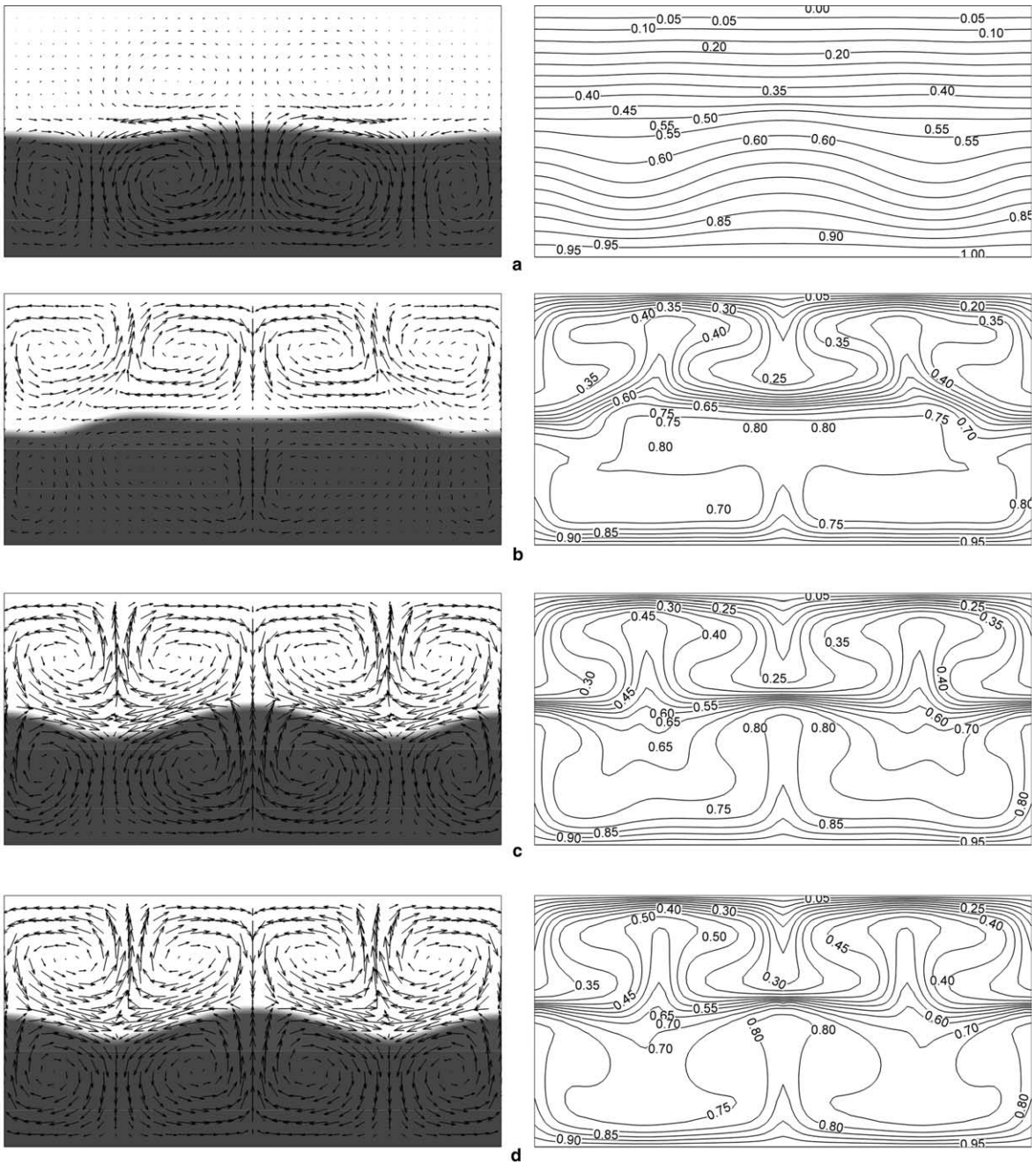

Fig. 4. Evolution of fluid flow and thermal fields $Ra_1 = 8.0 \times 10^4$, $Ca_1 = 4.6 \times 10^{-4}$ and $Ma_1 = 0$, $\varepsilon_1 = 0.26$: (a) $t = 65$, (b) $t = 130$, (c) $t = 200$ and (d) $t = 720$.

As the Rayleigh number is increased, the temperature gradient near the top wall, bottom wall and interface becomes sharper. The heat transfer rate is estimated in terms of the Nusselt number. The local Nusselt number and the average value are calculated as

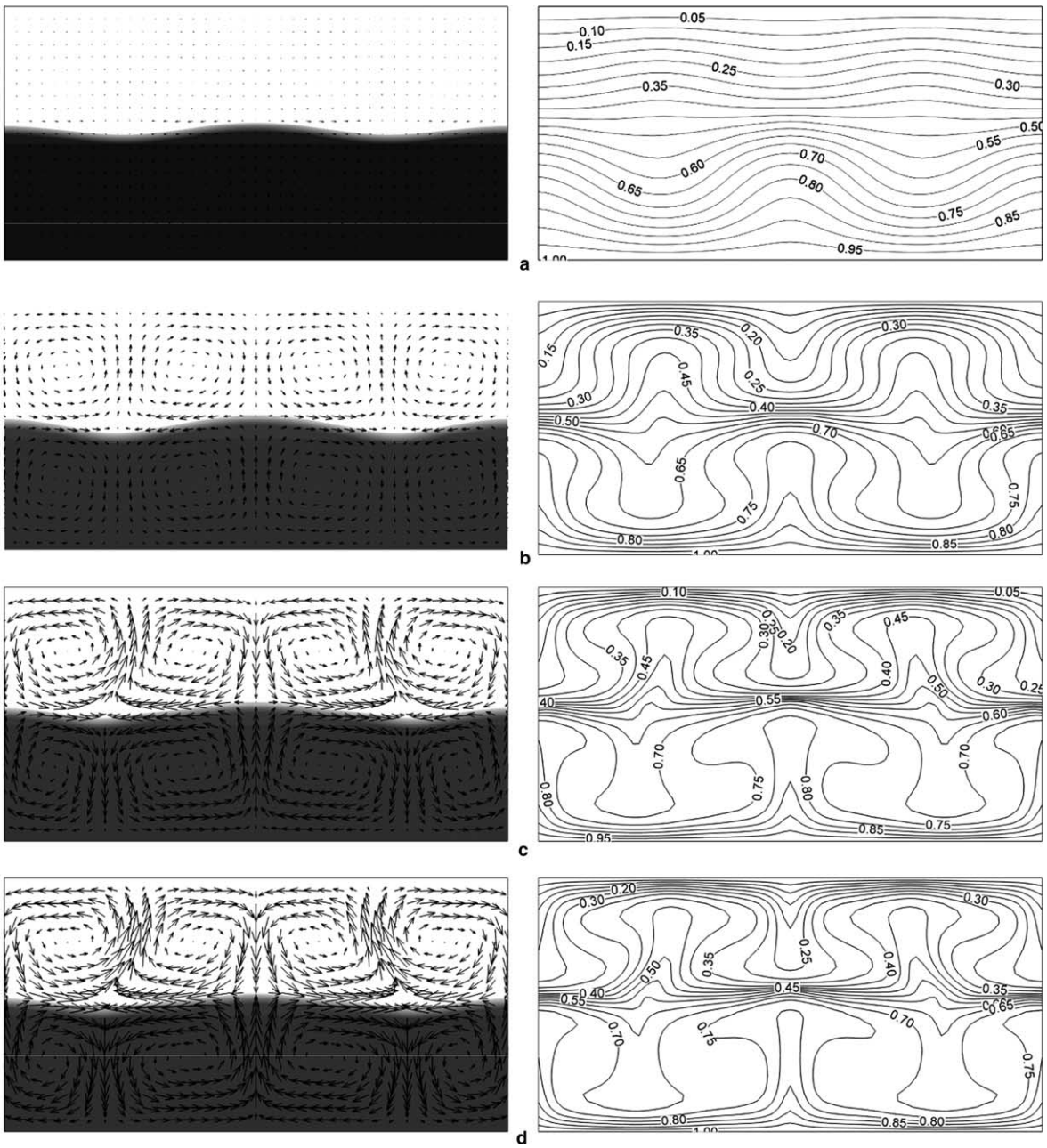

Fig. 5. Flow and thermal fields for $\varepsilon_1 = 0.15$, $Ca_1 = 4.6 \times 10^{-4}$ and $Ma_1 = 0$: (a) $Ra_1 = 6.0 \times 10^3$, (b) $Ra_1 = 1.2 \times 10^3$, (c) $Ra_1 = 4.8 \times 10^3$ and (d) $Ra_1 = 8.0 \times 10^4$.

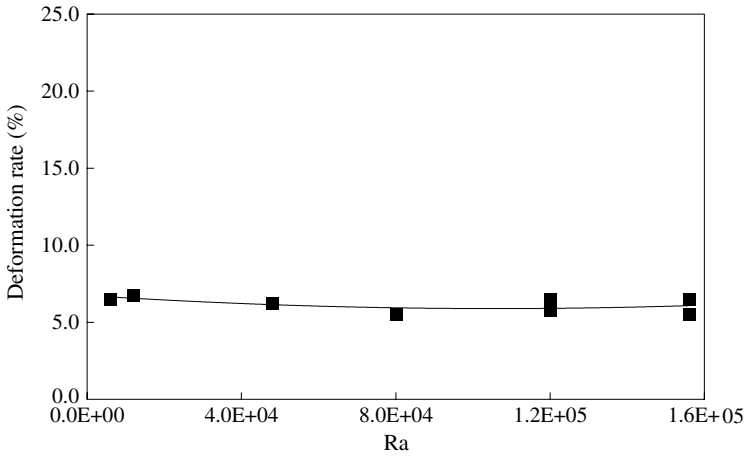

Fig. 6. Interface deformation vs. Ra $\varepsilon_1 = 0.15$, $Ca_1 = 4.6 \times 10^{-4}$ and $Ma_1 = 0$.

$$Nu = -\frac{H}{\Delta T}\left(\frac{\partial T}{\partial y}\right)_{\text{wall}}, \tag{38}$$

$$\bar{N}u = \frac{1}{W}\int_0^W Nu \cdot \mathrm{d}x, \tag{39}$$

where the temperature gradient $\partial T/\partial y$ is calculated using three points formula.

The local and average Nusselt numbers at the top and bottom wall along the x-axis are shown in Fig. 7. Locally, a double-peak occurs at the region corresponding maximum temperature gradient. The average Nusselt number is greatly altered by Rayleigh number value. The Nusselt numbers measured at the steady states are plotted in Fig. 8 as a function of Rayleigh number. The average Nusselt number increases with the Rayleigh number, as it does for single phase systems [28].

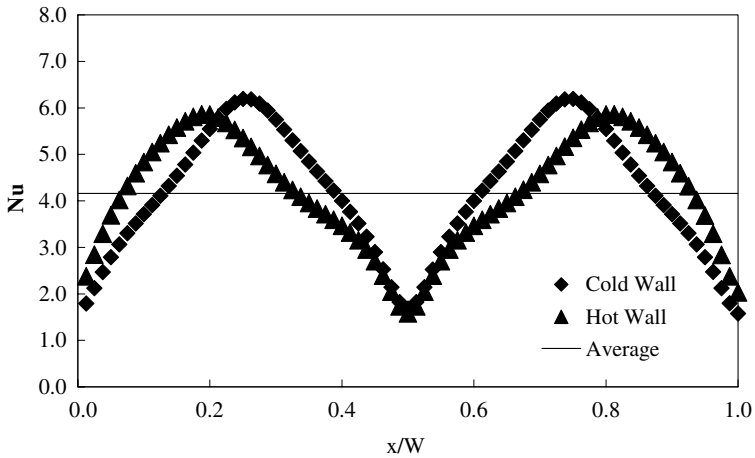

Fig. 7. Distribution of local Nusselt number along the cold and hot walls $\varepsilon_1 = 0.15$, $Ra_1 = 8.0 \times 10^4$, $Ca_1 = 4.6 \times 10^{-4}$ and $Ma_1 = 0$.

The effect of Capillary number Ca_1 on the interface deformation is illustrated by Fig. 9. Here, we fixed $\varepsilon_1 = 0.15$, $Ra_1 = 8.0 \times 10^4$ and neglected the interfacial force due to surface tension variation with temperature ($Ma_1 = 0$). For smaller Ca_1 number, the interface deformation increases rapidly as the Ca_1 number increases, until it approaches 3.7%. Subsequently, the interface deformation rate remains constant as the Ca_1 number is increased. Since the maximum deformation is only 3.7%, we conclude that changing Ca has a negligible effect on the interface deformation.

Finally, we examine the effect of the Marangoni number Ma_1 on the interface. We let the surface tension at the interface vary linearly with temperature. That is, the surface tension depends on temperature as

$$\sigma = \sigma_0 - \gamma \Delta T, \tag{40}$$

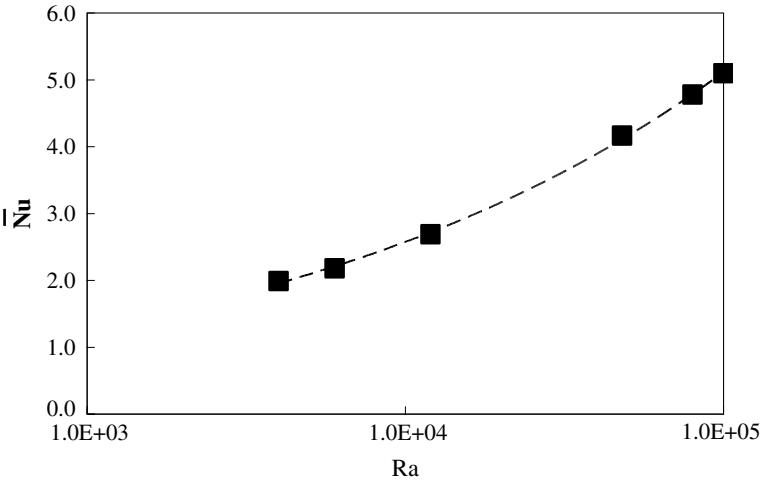

Fig. 8. The dependence of average Nusselt number on Rayleigh number $\varepsilon_1 = 0.15$, $Ca_1 = 4.6 \times 10^{-4}$ and $Ma_1 = 0$.

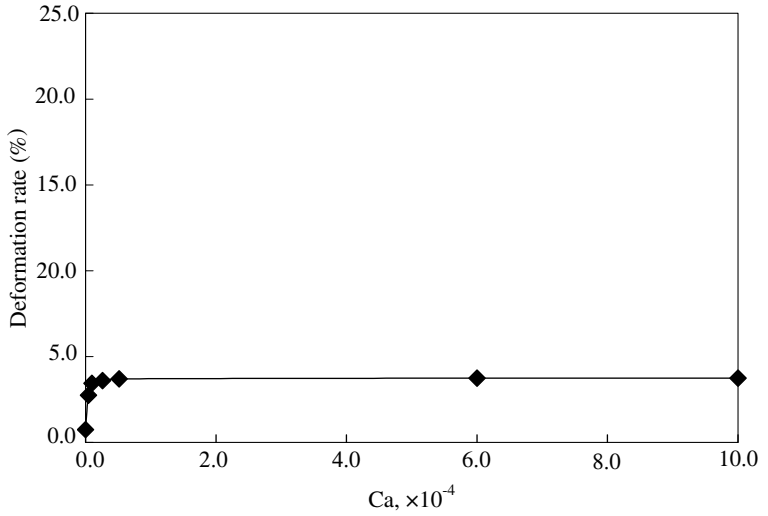

Fig. 9. Interface deformation vs. Capillary number $\varepsilon_1 = 0.15$, $Ra_1 = 8.0 \times 10^4$ and $Ma_1 = 0$.

where σ_0 is the surface tension at reference temperature T_0. The parameter γ is the absolute value of the derivative of the surface tension with respect to temperature, $d\sigma/dT$.

To determine the relationship between surface tension and parameter κ in Eq. (7), we conduct serial simulations for a static 2D circular bubble. According to the Laplace law, the pressure difference between the interior and the exterior of a static 2D circular bubble, $\Delta P = P_{in} - P_{ex}$, is related to the surface tension σ, through following rule:

$$\Delta P = \frac{\sigma}{r}, \tag{41}$$

where r is the bubble radius. Fig. 10 shows the measurements of $\Delta P/\kappa$ versus $1/r$ at the density ratio $\rho_r = 0.33$. We can fit the results to a linear equation as

$$\frac{\Delta P}{\kappa} = 0.043\frac{1}{r}, \tag{42}$$

Then the relation between surface tension and parameter κ can be written as

$$\sigma = 0.043\kappa \tag{43}$$

and

$$\gamma = \frac{d\sigma}{dT} = 0.043\frac{d\kappa}{dT}. \tag{44}$$

Because, for the problem under consideration, the temperature gradient is nearly perpendicular to the interface, the magnitude of the component of the temperature gradient along the interface is very small, even for large ε_1 values. It is observed that a change in Marangoni number will not bring about any significant change in the interface shape. An example is given in Fig. 11. Here, all parameters are set to the same value as the example given in Fig. 2(c), except for Ma_1. Compared with Fig. 2(c), the entire flow field tends to be excited. The thermocapillary force distorts the two pairs of convection rolls in the upper layer, and enlarges the center pair of convection rolls in the lower layer and ultimately squeezing the side pair of convection rolls to a strongly asymmetric vortex in each side. The corresponding temperature deviation from Fig. 2(c) is also shown in this figure. Fig. 12 depicts the corresponding Nusselt number along the top and bottom wall. Thermocapillary flow enhances the average Nusselt number slightly, from 4.16 to 4.4.

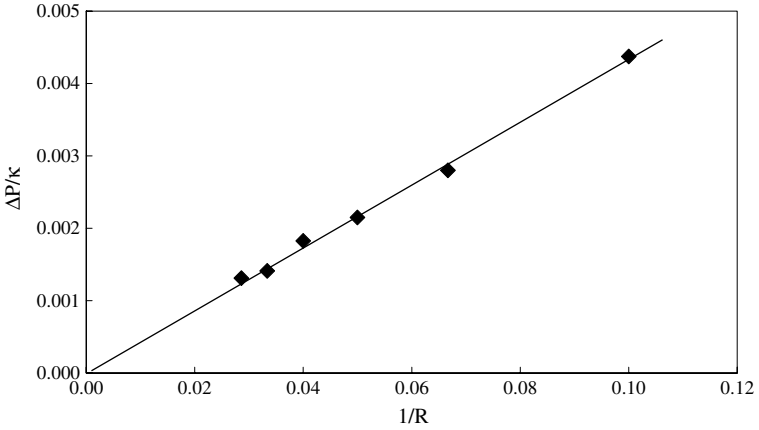

Fig. 10. Verification that calculated pressure differences fit the Laplace law.

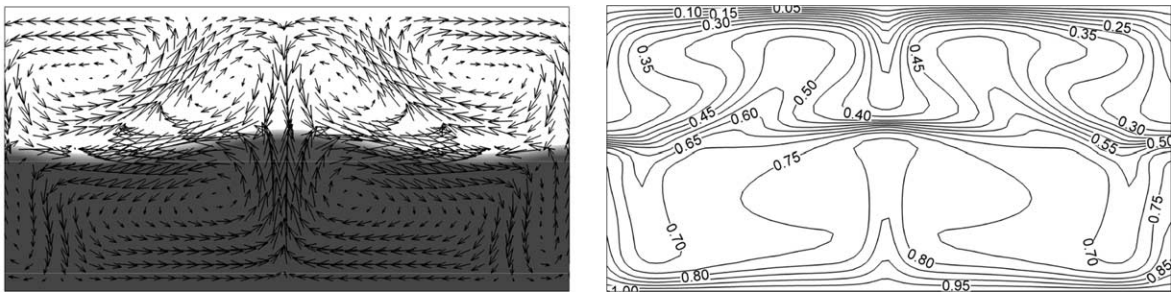

Fig. 11. Flow and thermal fields for $\varepsilon_1 = 0.15$, $Ca_1 = 4.6 \times 10^{-4}$, $Ma_1 = 8.6 \times 10^5$ and $Ra_1 = 8.0 \times 10^4$.

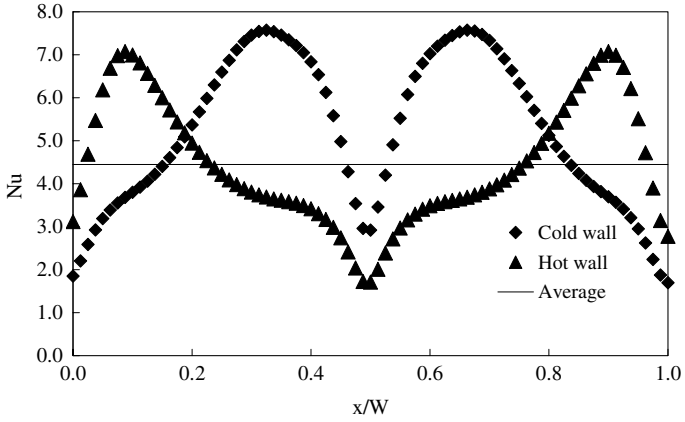

Fig. 12. Distribution of local Nusselt number along the cold and hot walls $\varepsilon_1 = 0.15$, $Ca_1 = 4.6 \times 10^{-4}$, $Ma_1 = 8.6 \times 10^5$ and $Ra_1 = 8.0 \times 10^4$.

5. Conclusions

A thermal lattice Boltzmann model for two-phase fluid flow with a double population distribution functions has been developed. The key point for this scheme is combining a microscale description of the flow with a macroscopic energy transport equation. At the microscale level, a multiphase lattice Boltzmann model is adopted to calculate some macroscale variables, such as index function, density, velocity and pressure. The temperature field is simulated by an additional scalar energy transport equation with finite-difference scheme. The simulation of the 2D Rayleigh–Benard and Marangoni convection in two-layer system with this model is analyzed. The results indicate that the interface deformation is mainly dependent on ε_1, the product of the lower fluid's thermal expansion coefficient and the sytem's characteristic temperature difference.

The present algorithm has been tested on the well-known Rayleigh–Benard problem and it appears to lend itself well to problems involving complicated free surfaces and interface deformations. Because of the nature of the approximations used to create a two-phase liquid the simulations are valid provided the density difference between the two fluids is small. The latter restriction was accepted only for convenience and other approaches for dealing with phases with large density differences are available but are more computationally intensive. The lattice Boltzmann method offers some advantages for problems involving multiphase fluids and is also readily adapted to complex geometries [29,30]. Thus, it can be

expected that the LBM will emerge as a popular method for dealing with multiphase flows in complex geometries.

Acknowledgments

The authors acknowledge support from the National Aeronautics and Space Administration through NASA Grant NAG8-1727 and through the National Center for Space Exploration Research.

References

[1] G. Ahlers, Experiments with pattern-forming system, Physica D 51 (1991) 421.
[2] M.C. Cross, P.C. Hohenberg, Pattern formation outside of equilibrium, Rev. Mod. Phys. 65 (1993) 851.
[3] R.M. Clever, F.H. Busse, Transition to time-dependent convection, J. Fluid Mech. 65 (1974) 625.
[4] T. Watanable, Flow pattern and heat transfer rate in Rayleigh–Benard convection, Phys. Fluids 16 (2004) 972.
[5] Ch. Jing, T. Sato, N. Imaishi, Rayleigh–Marangoni thermal instability in two-liquid layer system, Microgr. Sci. Technol. X (1) (1997).
[6] A. Prakash, J.N. Koster, Steady Rayleigh–Benard convection in a two-layer system of immiscible liquids, J. Heat Transf. 118 (1996) 366.
[7] P. Colinet, J.C. Legros, On the Hopf bifurcation occurring in the two-layer Rayleigh–Benard convection instability, Phys. Fluids 6 (1994) 2631.
[8] Y.Q. Zhang, J.I.D. Alexander, Surface tension and buoyancy-driven flow in a nonisothermal liquid bridge, Int. J. Numer. Meth. Fluids 14 (1992) 197–216.
[9] S.J. Tavener, K.A. Cliffe, Two-fluid Marangoni–Benard convection with a deformable interface, J. Comput. Phys. 182 (2002) 277.
[10] D.H. Rothman, S. Zaleski, Lattice-gas models of phase separation: interface, phase transitions and multiphase flow, Rev. Mod. Phys. 66 (1994) 1417.
[11] A.K. Gunstensen, D.H. Rothman, S. Zaleski, G. Zanetti, Lattice Boltzmann model of immiscible fluids, Phys. Rev. A 43 (1991) 4320.
[12] D. Grunau, S. Chen, K. Eggert, A lattice Boltzmann model for multiphase fluid flows, Phys. Fluids A 5 (1993) 2557.
[13] X. Shan, H. Chen, Lattice Boltzmann model for simulating flows with multiple phases and components, Phys. Rev. E 47 (1993) 1815.
[14] X. Shan, H. Chen, Simulation of non-ideal gases and liquid–gas phase transitions by the lattice Boltzmann equation, Phys. Rev. E 49 (1994) 2941.
[15] M.R. Swift, W.R. Osborn, J.M. Yeomans, Lattice Boltzmann simulation of nonideal fluids, Phys. Rev. Lett. 75 (1995) 830.
[16] M.R. Swift, E. Orlandini, W.R. Osborn, J.M. Yeomans, Lattice Boltzmann simulation of liquid–gas and binary-fluid system, Phys. Rev. E 54 (1996) 5041.
[17] Xiaoyi He, Shiyi Chen, Raoyang Zhang, A lattice Boltzmann scheme for incompressible multiphase flow and its application in simulation of Rayleigh–Taylor instability, J. Comput. Phys. 152 (1999) 642.
[18] Xiaoyi He, G.D. Doolen, Thermodynamic foundations of kinetic theory and lattice Boltzmann models for multiphase flows, J. Statist. Phys. 107 (1/2) (2002) 309.
[19] Shuling Hou, Xiaowen Shan, et al., Evaluation of two lattice Boltzmann models for multiphase flows, J. Comput. Phys. 138 (1997) 695.
[20] F.J. Alexander, S. Chen, J.D. Sterling, Lattice Boltzmann thermo-hydrodynamics, Phys. Rev. E 47 (1993) R2249.
[21] P. Pavlo, G. Vahala, L. Vahala, M. Soey, Linear stability analysis of thermo-lattice Boltzmann models, J. Comput. Phys. 139 (1998) 79.
[22] B.J. Palmer, D.R. Rector, Lattice–Boltzmann algorithm for simulating thermal two-phase flow, Phys. Rev. E 61 (5) (2000) 5295.
[23] O. Filipova, D. Hanel, A novel lattice BGK approach for low Mach number combustion, J. Comput. Phys. 158 (2000) 139.
[24] P.L. Bhatnagar, E.P. Gross, M. Krook, A model for collision processes in gases, I: Small amplitude processes in charged and neutral one component system, Phys. Rev. 94 (1954) 511.
[25] S. Chapman, T.G. Cowling, The Mathematical Theory of Non-uniform Gases, Cambridge University Press, 1970.
[26] C. Cercignani, Theory and Application of the Boltzmann Equation, Scottish Academic Press, 1975.
[27] D.D. Joseph, Y. Renardy, Fundamental of Two-Fluid Dynamics, Part II: Lubricated Transport, Drops and Miscible Liquids, Springer-Verlag, 1993.

[28] J.E. Fromm, Numerical solutions of the nonlinear equations for a heated fluid layer, Phys. Fluids 8 (1965) 1757.
[29] C. Shu, Y.T. Chew, X.D. Niu, Least-squares-based lattice Boltzmann method: a meshless approach for simulation of flows with complex geometry, Phys. Rev. E 64 (4) (2001) 045701.
[30] N.S. Martys, Hudong Chen, Simulation of multicomponent fluids in complex three-dimensional geometries by the lattice Boltzmann method, Phys. Rev. E 53 (1) (1996) 743.